



1 **Impacts of Cloud Microphysics Parameterizations on Simulated Aerosol-Cloud-**
2 **Interactions for Deep Convective Clouds over Houston**

3

4 Yuwei Zhang^{1,2}, Jiwen Fan^{2,*}, Zhanqing Li¹, Daniel Rosenfeld³

5

6 ¹Department of Atmospheric and Oceanic Science, University of Maryland, College Park, MD,
7 USA

8 ²Atmospheric Sciences and Global Change Division, Pacific Northwest National Laboratory,
9 Richland, WA, USA

10 ³ Institute of Earth Sciences, The Hebrew University of Jerusalem, Jerusalem, Israel

11 * *Correspondence to:* Jiwen Fan (jiwen.fan@pnnl.gov)

12

13



14 **Abstract**

15 Aerosol-cloud interactions remain largely uncertain in predicting their impacts on weather and
16 climate. Cloud microphysics parameterization is one of the factors leading to the large uncertainty.
17 Here we investigate the impacts of anthropogenic aerosols on the convective intensity and
18 precipitation of a thunderstorm occurring on 19 June 2013 over Houston with the Chemistry
19 version of Weather Research and Forecast model (WRF-Chem) using the Morrison two-moment
20 bulk scheme and spectral-bin microphysics (SBM) scheme. We find that the SBM predicts a deep
21 convective cloud agreeing better with observations in terms of reflectivity and precipitation
22 compared with the Morrison bulk scheme that has been used in many weather and climate models.
23 With the SBM scheme, we see a significant invigoration effect on convective intensity and
24 precipitation by anthropogenic aerosols mainly through enhanced condensation latent heating (i.e.,
25 the warm-phase invigoration). Whereas such effect is absent with the Morrison two-moment bulk
26 microphysics, mainly due to limitations of the saturation adjustment approach for droplet
27 condensation and evaporation calculation.

28



29 **1 Introduction**

30 Deep convective clouds (DCCs) produce copious precipitation and play important roles in
31 the hydrological and energy cycle as well as regional and global circulation (e.g., Arakawa, 2004;
32 Houze, 2014). DCCs and associated precipitation are determined by water vapor, vertical motion
33 of air, and cloud microphysics that could be affected by aerosols through aerosol-radiative
34 interactions (ARI) or aerosol-cloud interactions (ACI) or both. The cloud-mediated aerosol effects
35 are recognized by the Intergovernmental Panel on Climate Change (IPCC) as one of the key
36 sources of uncertainty in our knowledge of Earth's energy budget and anthropogenic climate
37 forcing (e.g., Arakawa, 2004; Andreae et al., 2005; Haywood and Boucher, 2000; Lohmann and
38 Feichter, 2005).

39 Precipitation, latent heat, and cloud radiative forcing associated with DCCs are strongly
40 associated with cloud microphysical processes, which can be modulated by aerosols through
41 serving as cloud condensation nuclei (CCN) and ice nuclei (IN). For aerosol-DCC interactions, a
42 well-known theory is that increasing aerosol concentrations can suppress warm rain as a result of
43 increased droplet number but reduced droplet size. This allows more cloud water to be lifted to a
44 higher altitude wherein the freezing of this larger amount of cloud water induces larger latent
45 heating associated with stronger ice microphysical processes, thereby invigorating convective
46 updrafts (referred to as “cold-phase invigoration,”; Khain et al. 2005; Rosenfeld et al., 2008). It is
47 significant in the situations of warm-cloud bases ($> 15^{\circ}\text{C}$; Fan et al., 2012b; Li et al., 2011;
48 Rosenfeld et al., 2014) and weak wind shear (Fan et al., 2009, 2012b, 2013; Li et al., 2008; Lebo
49 et al., 2012). Another theory is that increasing aerosols enhances droplet nucleation particularly
50 secondary nucleation after warm rain initiates, which promotes condensation because of larger
51 integrated droplet surface area associated with a higher number of small droplets (Fan et al., 2007,



52 2013, 2018; Koren et al., 2014; Lebo, 2018; Sheffield et al., 2015). This so-called “warm-phase
53 invigoration” , which is manifested in a warm, humid, and clean environment under which the
54 addition of a large number of ultrafine aerosol particles from urban pollution leads to stronger
55 invigoration than the “cold-phase invigoration” (Fan et al., 2018). Many factors can affect whether
56 aerosols invigorate or suppress convective intensity through ACI, such as environmental wind
57 shear (Fan et al., 2009; Lebo et al., 2012), relative humidity (Fan et al., 2007; Khain et al., 2008),
58 and Convective Available Potential Energy (Lebo et al., 2012; Morrison, 2012; Storer et al., 2010).
59 For DCCs with complicated dynamics, thermodynamics, and microphysics, aerosol impacts are
60 extremely complex and still remain poorly known.

61 Modeling of ACI is quite dependent on cloud microphysics parameterization schemes (e.g.,
62 Fan et al., 2012a; Khain and Lynn, 2009; Khain et al., 2009, 2015; Lebo and Seinfeld, 2011; Lee
63 et al., 2018; Loftus and Cotton, 2014; Wang et al., 2013). Two-moment bulk and bin schemes have
64 been widely used in ACI studies (e.g., Chen et al., 2011; Fan et al., 2013; Khain et al., 2010). In
65 two-moment bulk schemes, hydrometeor size distributions are diagnosed from the predicted
66 number and mass with an assumed spectral shape (e.g., gamma function). Saturation adjustment
67 approach is often used for calculating condensation and evaporation, meaning supersaturation and
68 undersaturation with respect to water are removed in cloud within a timestep. In bin schemes, the
69 size distributions of hydrometeors are discretized by a number of size bins and predicted, which
70 represents some aerosol-cloud interaction processes more physically compared with bulk schemes
71 (Fan et al., 2016; Khain et al., 2015).

72 Many studies have shown that bulk schemes are limited in representing certain important
73 microphysical processes such as aerosol activation, condensation, deposition, sedimentation, and
74 rain evaporation (Ekman et al., 2011; Khain et al., 2009; Lee et al. 2018; Li et al., 2009; Milbrandt



75 and Yau, 2005; Morrison, 2012; Wang et al., 2013). Though bin cloud microphysics can provide
76 a more rigorous numerical solution and a more robust cloud microphysics representation than
77 typical bulk microphysics, it is often applied in simulations for process understanding but rarely
78 in operational applications due to the expensive computation cost. For not introducing further
79 computation cost, bins schemes are also often run with a prescribed aerosol spectrum assuming a
80 fixed composition and a simple aerosol budget treatment without coupling with chemistry/aerosol
81 calculations. As a result, many aerosol life cycle processes such as aerosol nucleation, growth,
82 aqueous chemistry, aerosol resuspension, and below-cloud wet removal are missing or crudely
83 parameterized. Therefore, it is difficult to simulate spatial and temporal variabilities of aerosol
84 chemical composition and size distribution. In Gao et al. (2016), we have coupled a spectral-bin
85 microphysics scheme (SBM; Fan et al., 2012a; Khain et al., 2004) with the Chemistry version of
86 Weather Research and Forecast model (WRF-Chem; Grell et al., 2005; Skamarock et al., 2008),
87 called WRF-Chem-SBM, to address above-mentioned limitations. In this new model, the SBM
88 was coupled with the Model for Simulating Aerosol Interactions and Chemistry (MOSAIC; Fast
89 et al., 2006; Zaveri et al., 2008). The newly coupled system was initially evaluated for warm
90 marine stratocumulus clouds and showed much improved simulation of cloud droplet number
91 concentration and liquid water content compared with the default Morrison two-moment bulk
92 scheme (Gao et al., 2016).

93 The Houston area in summer, where isolated convective clouds with very warm cloud-bases
94 often occurred in the afternoon (Yuan et al., 2008), offers (a) a combination of polluted aerosols
95 from the urban and industrial area of Houston with significantly low background aerosol
96 concentrations surrounding Houston, (b) aerosol sources that are not correlated with meteorology,
97 and (c) weak synoptic forcing along with strong local triggering in the form of land-sea contrasts



98 and sea breeze fronts. This combination allows the manifestation of potentially large aerosol
99 effects. In this study, we choose a sea-breezed induced DCC case occurring 19-20 June 2013 near
100 Houston to (1) evaluate the performances of WRF-Chem-SBM in simulating deep convective
101 clouds and (2) gain a better understanding of the differences in aerosol effects predicted by SBM
102 and the Morrison two-moment bulk scheme as well as the major factors/processes responsible for
103 the differences. Considering that the convective clouds over the Houston area are mainly impacted
104 by the aerosols produced from anthropogenic activities, we focus on the anthropogenic aerosol
105 effect in this study. The simulated storm case is the same as the case for the Aerosol-Cloud-
106 Precipitation-Cloud (ACPC) Model Intercomparison Project (Rosenfeld et al., 2014;
107 www.acpcinitiative.org).

108 **2 Case Description and Observational Data**

109 A local convective event near Houston, Texas on 19-20 June 2013 is selected for the study
110 owing to the most favorable conditions for simulating isolated convective cells. As above-
111 mentioned, the case is also selected for the ACPC Model Intercomparison Project
112 (www.acpcinitiative.org). The isolated relatively weak convective clouds started from the late
113 morning because of a trailing front. With increased solar radiation in early afternoon and
114 strengthening of a sea breeze circulation that transports warm and humid air from the Gulf of
115 Mexico to Houston urban area, deep convective cells over Houston and Galveston bay areas
116 developed (Fig. 1). The strong convective cell observed near the Houston city was initiated around
117 2145 UTC (local time 16:45), and developed to its peak precipitation at 2217 UTC based on radar
118 observation (Fig. 1). The maximum reflectivity was more than 55 dBZ. This storm cell lasted for
119 about 1.5 hours.



120 We used the following observation data for model evaluation. Particulate matter (PM) 2.5
121 data provided by Texas Commission for Environmental Quality (TCEQ) at
122 <https://www.tceq.texas.gov/agency/data/pm25.html> are used to evaluate the simulated aerosols
123 near the surface. The data for evaluating cloud base heights and CCN number concentration at
124 cloud base are obtained from the Visible Infrared Imaging Radiometer Suite (VIIRS) retrievals
125 based on the method of Rosenfeld et al., (2016). The 2-m temperature and 10-m winds are from
126 the North American Land Data Assimilation System (NLDAS) with 0.125-deg resolution at
127 <https://climatedataguide.ucar.edu/climate-data/nldas-north-american-land-data-assimilation->
128 system. The observed radar reflectivity is used to evaluate the simulated convective system. The
129 radar reflectivity is obtained from Next-Generation Weather Radar (NEXRAD) network at
130 <https://www.ncdc.noaa.gov/data-access/radar-data/nexrad-products>, with a temporal frequency of
131 every ~ 5 minutes and 1 km horizontal spatial resolution.

132 **3. Model description and experiments**

133 We conducted model simulations using the version of WRF-Chem based on Gao et al.
134 (2016) coupling with the Morrison two-moment scheme (Morrison et al., 2005; Morrison et al.,
135 2009; Morrison and Milbrandt, 2011) and SBM (Khain et al., 2004; Fan et al., 2012). The version
136 of SBM employed in this study is a fast version of the Hebrew University Cloud Model (HUCM)
137 described by Khain et al. (2004) with improvements from Fan et al. (2012a) and (2017). The
138 considered hydrometer size distributions are droplets/raindrops, cloud ice/snow and graupel. The
139 graupel version is used because it is more appropriate for simulating the convective storm over the
140 Houston area than the hail version. SBM is currently coupled with the four-sector version of
141 MOSAIC (0.039-0.156, 0.156-0.624, 0.624-2.5 and 2.5-10.0 μm). As detailed in Gao et al. (2016),
142 the aerosol processes including aerosol activation, resuspension, and in-cloud wet-removal are also



143 improved. Theoretically, both aerosol and cloud processes can be more realistically simulated
144 particularly under the conditions of complicated aerosol compositions and aerosol spatial
145 heterogeneity compared with original WRF-Chem. The dynamic core of WRF-Chem-SBM is the
146 Advanced Research WRF model that is fully compressible and nonhydrostatic with a terrain-
147 following hydrostatic pressure vertical coordinate (Skamarock et al., 2008). The grid staggering is
148 the Arakawa C-grid. The model uses the Runge-Kutta 3rd order time integration schemes, and the
149 3rd and 5th order advection schemes are selected for the vertical and horizontal directions,
150 respectively. The positive definite option is employed for advection of moist and scalar variables.

151 Two nested domains with horizontal grid spacings of 2 and 0.5 km and horizontal grid points
152 of 450×350 and 500×400 for Domain 1 and Domain 2, respectively, are used (Fig. 2a), with 51
153 vertical levels up to 50 hPa. The chemical and aerosol lateral boundary and initial conditions for
154 Domain 1 simulations were from a quasi-global WRF-Chem simulations at 1-degree grid spacing,
155 and meteorological lateral boundary and initial conditions were created from MERRA-2 (Gelaro
156 et al., 2017). Two simulations were run over Domain 1 with anthropogenic emissions turned on
157 and off, respectively, to provide two different aerosol scenarios for the initial and boundary
158 chemical and aerosol conditions for Domain 2 simulations: (1) a polluted aerosol scenario with
159 anthropogenic aerosols accounted which is for the real situation; (2) an assumptive clean scenario
160 without anthropogenic aerosols. Domain 2 is run with initial and lateral boundary chemical and
161 aerosols fields from Domain 1 outputs and initial and lateral boundary meteorological conditions
162 from MERRA-2. Note that we use the meteorology from MERRA-2 as the initial and lateral
163 boundary conditions for Domain 2 instead of Domain 1 outputs, because we want to keep the
164 initial and lateral boundary meteorological conditions the same for all the sensitivity tests with



165 different microphysics and aerosol setups (meteorology is different between the two simulations
166 over Domain 1).

167 The simulations in Domain 1 were initiated at 0000 UTC on 14 Jun and ended at 1200 UTC
168 20 June with about 5 days for the chemistry spin-up. The meteorological field was reinitialized
169 every 36 hours to prevent the model drifting. The dynamic time step was 6 s for Domain 1 and 3
170 s for Domain 2. The anthropogenic emission was from NEI-2011 emissions. The biogenic
171 emission came from the Model of Emissions of Gases and Aerosols from Nature (MEGAN)
172 product (Guenther et al., 2006). The biomass burning emission was from the Fire Inventory from
173 NCAR (FINN) model (Wiedinmyer et al., 2011). We used the Carbon Bond Mechanism Z
174 (CBMZ) gas-phase chemistry (Zaveri and Peters, 1999) and MOSAIC aerosol model with four
175 bins (Zaveri et al., 2008). The physics schemes other than microphysics applied in the simulation
176 are the Unified Noah land surface scheme (Chen and Dudhia, 2001), Mellor-Yamada-Janjic
177 planetary boundary layer scheme (Janjic et al., 1994), Multi-layer, Building Environment
178 Parameterization (BEP) urban physics scheme (Salamanca and Martilli, 2010), the RRTMG
179 longwave and shortwave radiation schemes (Iacono et al., 2008).

180 The main purpose of the simulations in Domain 1 is to provide initial and boundary chemical
181 and aerosol conditions for the simulations in Domain 2. To save computational cost, WRF-Chem
182 coupled with Morrison two-moment bulk microphysics scheme (Morrison et al., 2005) is used for
183 the simulations in Domain 1. Two simulations run for Domain 1 are referred to as D1_MOR_anth
184 in which the anthropogenic emissions are turned on and D1_MOR_noanth where the
185 anthropogenic emissions are turned off. Then four major experiments are carried out to simulate
186 the convective event near the Houston over Domain 2 with two cloud microphysics schemes and
187 two aerosol scenarios, respectively. We refer to the simulation in which SBM is used and the



188 anthropogenic emissions are included using the initial and boundary chemicals and aerosols from
189 D1_MOR_anth, as our baseline simulation (referred to as “SBM_anth”). SBM_noanth is based on
190 SBM_anth but uses initial and boundary chemicals and aerosols from D1_MOR_noanth and turns
191 off the anthropogenic emissions, meaning that anthropogenic aerosols are not taken into account.
192 MOR_anth and MOR_noanth are the two corresponding simulations to SBM_anth and
193 SBM_noanth, respectively, using the Morrison two-moment bulk microphysics scheme. To
194 examine the contribution of the saturation adjustment approach for condensation and evaporation
195 to the simulated aerosol effects with the Morrison scheme, we further conducted two sensitivity
196 tests, based on MOR_anth and MOR_noanth, by replacing the saturation adjustment approach in
197 the Morrison scheme with the condensation and evaporation calculation based on an explicit
198 representation of supersaturation over a time step as described in Lebo et al. (2012). Note in
199 both SBM and this modified Morrison schemes, the supersaturation for condensation and
200 evaporation are calculated after the advection. These two simulations are referred to as
201 MOR_SS_anth and MOR_SS_noanth, respectively. To present more robust results, we carry out
202 a small number of ensembles (three) for each case over Domain 2 (we do not have computer time
203 to do more ensemble runs). The three ensemble runs are only different in the initialization time:
204 0000 UTC, 0600 UTC, and 1200 UTC on 19 June. All the simulations end at 1200 UTC 20 June.
205 All analysis results for Domain 2 simulations in this study are the mean values of three ensemble
206 runs.

207 We evaluate the aerosol and CCN properties simulated by D1_MOR_anth to ensure realistic
208 aerosol fields, which are used for the Domain 2 simulations with anthropogenic aerosols
209 considered. These evaluations are included in the section 4.1.



210 From D1_MOR_anth simulation, we see a very large spatial variability of aerosol number
211 concentrations (Fig. 2b). There are three regions with significantly different aerosol loadings over
212 the domain as shown by the black boxes in Fig. 2b: (a) the Houston urban area, (b) the rural area
213 about 100 km northeast to Houston, and (c) Gulf of Mexico. Aerosols over the Houston urban area
214 are mainly contributed by organic aerosols, which are highly related with industrial and ship
215 channel emissions. The rural area aerosols are mainly from sulfate and sea salt aerosol is the major
216 contributor over the Gulf of Mexico. This suggests that aerosol properties are extremely
217 heterogenous in this region. The aerosols over Houston urban area are generally about 5 and 10
218 times higher than the rural and Gulf area, respectively (Fig. 2c). The size distributions show a
219 three-mode distribution with the largest differences from the Aitken mode (peaks at 50 nm; Fig.
220 2c). These ultrafine aerosol particles are mainly contributed by anthropogenic activities (Fig. 2b,
221 d). With the anthropogenic emissions turned off, the simulated aerosols are much lower and have
222 much less spatial variability (Fig. 2d).

223 4 Result

224 4.1 Model Evaluation

225 We first show the evaluation of the aerosol and CCN properties simulated by
226 D1_MOR_anth, which runs over Domain 1, much larger than Domain 2. As described in Table 1,
227 there are eight PM monitoring sites from TCEQ around the Houston area. Surface PM_{2.5} shows
228 high concentrations at Houston and its downwind regions (Fig. 3). The values from
229 D1_MOR_anth show a very good agreement with the observations in terms of the surface PM_{2.5}
230 averaged over 24 hours (the day before the convection near Houston). The hourly variations of
231 ground-level PM_{2.5} concentrations from both observation and D1_MOR_anth for these sites in



232 the day before the convective initiation is depicted in Fig. 4. Generally, the simulated hourly
233 pattern agrees with the observation for eight stations. D1_MOR_anth reproduces the diurnal
234 variations, especially the increasing trend from 1200 UTC to 1800 UTC 19 Jun prior to the
235 initiation of deep convective cells over Houston and Galveston bay areas.

236 The evaluation of the cloud base heights and CCN at cloud bases at the warm cloud stage
237 before transitioning to deep clouds (2000 UTC) are shown in Fig.5. Over the Houston and its
238 surrounding area (black box in Fig. 5), the simulated cloud base heights are about 1.5-2 km, in an
239 agreement with the retrieved values from VIIRS satellite, which are around 1.2-1.8 km (Fig. 5a-
240 b). The retrieved CCN concentrations at cloud bases vary significantly over the domain and this
241 spatial variability is generally captured by the model (Fig. 5c-d). For example, D1_MOR_anth
242 simulates some high CCN concentrations ($400\text{-}800\text{ cm}^{-3}$ with some above 1000 cm^{-3}) over the
243 Houston and around the Bay area, relatively low CCN values at the rural areas (about $200\text{-}600\text{ cm}^{-3}$)
244 and very low values over the Gulf of Mexico (less than 200 cm^{-3}), as shown in Fig. 5d. This is
245 consistent with the spatial variability from the retrievals (Fig. 5c). The evaluation of aerosol
246 properties before the initiation of Houston convective cells and CCN at the warm cloud stage
247 before transitioning to deep clouds provides us confidence in using the chemical and aerosol fields
248 from Domain 1 outputs to feed Domain 2 simulations.

249 Now we are evaluating near-surface temperature and winds, reflectivity and precipitation
250 simulated by SBM_anth and MOR_anth. Fig. 6 shows the comparisons in 2-m temperature and
251 10-m winds at 1800 UTC (before the convective initiation). Both SBM_anth and MOR_anth
252 capture the general temperature pattern with a little overestimation at the northeast part of the
253 domain (mainly rural area). SBM_anth predicts a slightly higher temperature than MOR_anth in
254 the northern part of the Houston region (purple box in Fig. 6), which agrees with NLDAS better.



255 SBM_anth gets the similar southerly winds from Gulf of Mexico to Houston as shown in NLDAS,
256 while the southerly winds from Gulf of Mexico become very weak or disappear prior to reaching
257 Houston in MOR_anth.

258 For the Houston convective cell that we focused (red box in Fig. 7a), SBM_anth simulates
259 it well in both location and high reflectivity value (greater than 50 dBZ) in comparison with the
260 NEXRAD observation (Fig. 7a-b). The simulated composite reflectivities (i.e., the column
261 maximum) are up to 55-60 dBZ, consistent with NEXRAD. With the Morrison scheme,
262 MOR_anth simulates several small convective cells near Houston with maximum reflectivity of
263 55 dBZ or less (Fig. 7c). The contoured frequency by altitude diagram (CFAD) plots for the entire
264 storm period show that SBM_anth is in a better agreement with observation compared with
265 MOR_anth, especially for vertical structure of the high reflectivity range (greater than 48 dBZ,
266 black dashed lines in Fig. 8) and echo top heights, which can reach up to 14-15 km (Fig. 8a-b).
267 MOR_anth overestimates the occurrence frequencies of the 35-45 dBZ range and underestimates
268 those of the low and high reflectivity ranges (less than 15 dBZ or larger than 50 dBZ) as well as
269 the echo top heights (1-2 km lower than SBM_anth; Fig. 8c).

270 For the precipitation rates averaged over the study area (red box in Fig. 7), the observation
271 shows two peaks, which are captured by both SBM_anth and MOR_anth (Fig. 9a). However, the
272 timing for the first peak is about 30 and 60 min earlier in SBM_anth and MOR_anth than the
273 observation, respectively. Also, SBM_anth predicts the rain rate intensities at the two peak times
274 more consistent with the observations whereas MOR_anth underestimates the rain rate intensity at
275 the second peak time (Fig. 9a). The large precipitation rates (greater than 15 mm h⁻¹) in SBM_anth
276 has a ~1.5 times larger occurrence probability than those in MOR_anth, showing a better
277 agreement with the observation (Fig. 9b). Overall, the performance of SBM_anth is superior to



278 MOR_anth in simulating the location and intensity of the convective storm and associated
279 precipitation.

280 **4.2 Simulated Aerosol Effects on Cloud and Precipitation**

281 Now we look at the effects of anthropogenic aerosols on the deep convective storm
282 simulated with SBM and Morrison microphysics schemes. Fig. 9a shows that with the SBM
283 scheme, anthropogenic aerosols remarkably increase the mean surface rain rates (by ~30%; from
284 SBM_noanth to SBM_anth), mainly because of the increased occurrence frequency (nearly
285 doubled) for relatively large rain rates (i.e., 10-15 mm h⁻¹ and >15 mm h⁻¹) in Fig. 9b. With the
286 Morrison scheme, the changes in mean precipitation and the PDF from MOR_noanth to
287 MOR_anth are relatively small, showing a very limited aerosol effect on precipitation. With the
288 SBM scheme, the increase in the updraft speeds by the anthropogenic aerosols is even more notable
289 than the precipitation (Fig. 10a-b). Above 5-km altitude, the occurrence frequencies of updraft
290 speeds greater than 0.4% extend to a much larger values, with 36 m s⁻¹ at the upper levels in
291 SBM_anth while only ~ 20 m s⁻¹ in SBM_noanth. With the Morrison scheme, the changes are not
292 significant by the anthropogenic aerosols (MOR_noanth vs MOR_anth in Fig. 10c-d). From
293 MOR_noanth to MOR_anth, there is a slight increase in updraft speed at around 9-11 km altitudes
294 but a slight decrease at 6-8 km altitudes. The significant invigoration of convective intensity by
295 anthropogenic aerosols with the SBM scheme explains the much larger occurrences of relatively
296 large rain rates and overall more surface precipitation due to the anthropogenic aerosol effect (Fig.
297 9).

298 Now the question is why the anthropogenic aerosols enhance convective intensity of the
299 storm with the SBM scheme while the effect is very small with the Morrison scheme. Fig. 11
300 shows the vertical profiles of mean updraft velocity, thermal buoyancy, and total latent heating



301 rate of the top 25th percentile updrafts with value greater than 2 m s^{-1} during the deep convective
302 cloud stage. With the SBM microphysics scheme, the increased convective intensity due to
303 anthropogenic aerosol effect corresponds to the increased thermal buoyancy which is particularly
304 notable at upper levels ($\sim 20\%$) from SBM_noanth to SBM_anth (Fig. 11a, c). The increased
305 thermal buoyancy can be explained by the increased total latent heating (Fig. 11e), which is mainly
306 from the larger condensation latent heating (Fig. 12a). From SBM_noanth to SBM_anth, the latent
307 heating from ice-related microphysical processes (including deposition, drop freezing, and riming)
308 has a relatively smaller increase than that from condensation (about half of the increase in
309 condensation latent heating as shown in Fig. 12a). As shown in Fan et al., (2018), the increase in
310 lower-level condensation latent heating has a much larger effect on intensifying updraft intensity
311 compared with the same amount of increase in high-level latent heating from ice-related
312 microphysical processes. This suggests that the convective invigoration by the anthropogenic
313 aerosols with the SBM scheme should be mainly through the “warm-phase invigoration”
314 mechanism. Compared with the Morrison scheme, the increase of total latent heating by the
315 anthropogenic aerosols is almost doubled with the SBM scheme, explaining more remarkable
316 enhancement of thermal buoyancy and thus the convective intensity (red lines vs blue lines in Fig.
317 11). From MOR_noanth to MOR_anth, there is a small increase in both the condensation latent
318 heating and high-level latent heating associated with ice-related processes (blue lines in Fig. 12b).
319 The major difference in the increase of latent heating by the anthropogenic aerosols between SBM
320 and Morrison microphysics schemes comes from the condensation latent heating, with a $\sim 20\%$
321 increase with SBM but only $\sim 8\%$ with Morrison (Fig. 12). The lack of significant increase in
322 condensation latent heating limits the “warm-phase invigoration”, mainly responsible for the



323 limited aerosol impacts on convective intensity and associated precipitation with the Morrison
324 scheme.

325 To understand why the responses of condensation to the anthropogenic aerosols are
326 different between the SBM and Morrison schemes, we look into the process rates of drop
327 nucleation and condensation (Fig. 13). The calculations of aerosol activation and
328 condensation/evaporation in the SBM scheme are based on the Köhler theory and diffusional
329 growth equations in light of particle size and supersaturation, respectively. Whereas in the Morrison
330 scheme, the Abdul-Razzak and Ghan (2002) parameterization is used for aerosol activation and
331 the saturation adjustment method is applied for condensation and evaporation calculation. With
332 the SBM scheme, the anthropogenic aerosols increase the drop nucleation rates by a few times
333 over the profile (red lines in Fig. 13a), and the condensation rates are also drastically increased
334 (doubled between 4–6 km altitudes as shown in Fig. 13c). The enhanced condensation rate by the
335 anthropogenic aerosols is because much more aerosols are activated to form a larger number of
336 small droplets, increasing the integrated droplet surface area for condensation, as documented in
337 Fan et al., (2018). As a result, supersaturation is drastically lower in SBM_anth than SBM_noanth
338 (green lines in Fig. 13a). With the Morrison scheme, we still see a large increase in droplet
339 nucleation rate (Fig. 13b). However, the condensation rates are barely increased (blue solid vs.
340 dashed lines in Fig. 13d). We hypothesize that the lack of response of condensation to the increased
341 aerosol activation with the Morrison scheme is mainly because of the saturation adjustment
342 calculation of the condensation and evaporation process. The approach does not allow
343 supersaturation in cloud and the calculation does not depend on supersaturation, thus removes the
344 sensitivity to the anthropogenic aerosols.



345 To verify our hypothesis and examine how much the saturation adjustment method is
346 responsible for the weak responses of condensation latent heating and convection to the added
347 anthropogenic aerosols, we conducted two additional sensitivity tests by replacing the
348 saturation adjustment approach in Morrison scheme with the condensation and evaporation
349 calculation based on an explicit representation of supersaturation over a time step, as described
350 in Section 3. The result shows the Morrison scheme with the simple calculation of supersaturation
351 for condensational growth significantly changes the condensation rate (orange vs. blue lines in Fig.
352 13d) and a similarly large enhancement (from MOR_SS_noanth to MOR_SS_anth in Fig. 13d) is
353 seen as the SBM scheme (Fig. 13c). This leads to a larger increase in condensation latent heating
354 (orange lines in Figure 12b) compared with the original Morrison scheme, resulting a similarly
355 large increase in thermal buoyancy by the anthropogenic aerosols as with the SBM scheme (orange
356 lines in Fig. 11d), thus a similarly large increase in the convective intensity (orange lines in Fig.
357 11b). The increase of precipitation from MOR_SS_noanth to MOR_SS_anth is also similar to that
358 with the SBM scheme (not shown). These results verify that the saturation adjustment approach
359 for parameterizing condensation and evaporation is the major reason responsible for limited
360 aerosol effects on convective intensity and precipitation with the Morrison scheme. Past studies
361 also showed the limitations of the saturation adjustment approach in simulating aerosol impacts
362 on deep convective clouds (e.g., Fan et al., 2016; Lebo et al., 2012; Lee et al., 2018; Wang et al.,
363 2013).

364 Fig. 14 shows the responses of hydrometeor mass to anthropogenic aerosol effects. With
365 the SBM scheme, the increases of cloud mass, rain mass, and total ice mass (ice, snow, and graupel)
366 by the anthropogenic aerosols are very significant (Fig. 14, left), corresponding to convective
367 invigoration. The increase of the total ice mass is particularly significant (from 3.5 to 5.5 g kg⁻¹



368 around 10-km altitude), suggesting a large effect of enhanced convective intensity on ice
369 hydrometeors. However, with the Morrison scheme, little change is seen (Fig. 14, right, blue lines).
370 By replacing the saturation adjustment with a simple calculation based on supersaturation for
371 condensation and evaporation in the Morrison scheme, the increases in those hydrometeor masses
372 become as evident as those with the SBM scheme (Fig. 14, right, orange lines).

373 **5 Conclusions and Discussion**

374 We have conducted model simulations of a deep convective cloud case occurring on 19 June
375 2013 over the Houston area with WRF-Chem coupled with the SBM and Morrison microphysics
376 schemes to (1) evaluate the performance of WRF-Chem-SBM in simulating the deep convective
377 clouds, and (2) explore the differences in aerosol effects on the deep convective clouds produced
378 by the SBM and Morrison schemes and the major factors responsible for the differences.

379 We have evaluated the simulated aerosols, CCN, cloud base heights, reflectivity, and
380 precipitation. The model simulates the large spatial variability of aerosols and CCN from Gulf of
381 Mexico, rural area, to Houston city. On the bulk magnitudes, the model captures the surface PM_{2.5},
382 cloud base height, and CCN at cloud base near the Houston reasonably well. These realistically
383 simulated aerosol fields were fed to higher resolution simulations (0.5 km) using the SBM and
384 Morrison schemes. With the SBM scheme, the model simulates a deep convective cloud over the
385 Houston in a better agreement with the observed radar reflectivity and precipitation, compared
386 with using the Morrison scheme.

387 By excluding the anthropogenic aerosols in the simulations, the effects of anthropogenic
388 aerosols on the deep convective clouds and differences in aerosol effects using the two
389 microphysics schemes were examined. With the SBM scheme, anthropogenic aerosols notably
390 increase convective intensity, enhance the peak precipitation rate over the Houston area (by ~30%),



391 and double the frequencies of relatively large rain rates ($> 10 \text{ mm h}^{-1}$). The enhanced convective
392 intensity by anthropogenic aerosols makes the simulated storm agree better with the observed,
393 mainly attributed to the increased condensation latent heating, indicating the “warm-phase
394 invigoration”. In contrast, with the Morrison scheme, there is no significant anthropogenic aerosol
395 effect on the convective intensity and precipitation.

396 Sensitivity tests by replacing the saturation adjustment with the condensation and evaporation
397 calculation based on an explicit representation of supersaturation over a time step show the
398 similar aerosol effects on condensation, convective intensity, hydrometeor mass mixing ratios, and
399 precipitation as with the SBM scheme. Therefore, the saturation adjustment method for the
400 condensation and evaporation calculation is mainly responsible for the limited aerosol effects with
401 the Morrison scheme. This is because the saturation adjustment method does not allow for the
402 “warm-phase invigoration”, which is different from Lebo et al. (2012) showing that the saturation
403 adjustment artificially enhanced condensation latent heating at low levels and limited the potential
404 for aerosols to invigorate convection through the “cold-phase invigoration” mechanism in their
405 idealized simulations of a supercell storm with the thermal bubble initiation. In this study of the
406 thunderstorm with WRF real-case simulations for both chemistry/aerosols and clouds, the
407 saturation adjustment method actually leads to a smaller condensation latent heating than the
408 explicit calculation with supersaturation (solid bold blue vs. solid bold orange line in Fig. 12b).
409 Thus, when the computational resource is not sufficient or in other situations such as the
410 application of SBM is not available, the Morrison scheme modified with the condensation and
411 evaporation calculation based on a simple representation of supersaturation can be applied to study
412 aerosol effects on convective clouds, especially for warm and humid cloud cases in which the
413 response of condensation to aerosols is particularly important.



414 Following Fan et al., (2018), which showed that the “warm-phase invigoration” mechanism
415 was manifested by ultrafine aerosol particles in the Amazon warm and humid environment with
416 extremely low background aerosol particles. Here we showed that in summer anthropogenic
417 aerosols over the Houston area may also enhance the thunderstorm intensity and precipitation
418 through the same mechanism by secondary nucleation of numerous ultrafine aerosol particles from
419 the anthropogenic sources. But the magnitude of the effect is not as substantial as in the Amazon
420 environment. Possible reasons include that background aerosols are much higher over the Houston
421 area and air is not as humid as Amazon.

422 **Acknowledgments**

423 This study is supported by the U.S. Department of Energy Office of Science through its Early
424 Career Award Program and a grant DE-SC0018996 and the NSF (AGS1837811). PNNL is
425 operated for the US Department of Energy (DOE) by Battelle Memorial Institute under Contract
426 DE-AC05-76RL01830. This research used resources of PNNL Institutional Computing (PIC), and
427 the National Energy Research Scientific Computing Center (NERSC), a U.S. Department of
428 Energy Office of Science User Facility operated under contract DE-AC02-05CH11231. We thank
429 Chun Zhao at China University of Science and Technology for providing the quasi-global WRF-
430 Chem simulation data, and Hugh Morrison at the National Center for Atmospheric Research for
431 the Morrison code with supersaturation-forced condensation and evaporation calculation.

432

433



434 **Reference**

- 435 Abdul-Razzak, H., and Ghan, S. J.: A parameterization of aerosol activation - 3. Sectional
436 representation, *J Geophys Res-Atmos*, 107, 4026, doi: 10.1029/2001jd000483, 2002.
- 437 Andreae, M. O., Jones, C. D., and Cox, P. M.: Strong present-day aerosol cooling implies a hot
438 future, *Nature*, 435, 1187-1190, doi: 10.1038/nature03671, 2005.
- 439 Arakawa, A.: The cumulus parameterization problem: Past, present, and future, *J Climate*, 17,
440 2493-2525, doi: 10.1175/1520-0442(2004)017<2493:Ratcpp>2.0.Co;2, 2004.
- 441 Chen, F., and Dudhia, J.: Coupling an advanced land surface-hydrology model with the Penn State-
442 NCAR MM5 modeling system. Part I: Model implementation and sensitivity, *Mon*
443 *Weather Rev*, 129, 569-585, doi: 10.1175/1520-0493(2001)129<0569:Caalsh>2.0.Co;2,
444 2001.
- 445 Chen, Y. C., Xue, L., Lebo, Z. J., Wang, H., Rasmussen, R. M., and Seinfeld, J. H.: A
446 comprehensive numerical study of aerosol-cloud-precipitation interactions in marine
447 stratocumulus, *Atmos Chem Phys*, 11, 9749-9769, doi: 10.5194/acp-11-9749-2011, 2011.
- 448 Ekman, A. M. L., Engstrom, A., and Soderberg, A.: Impact of Two-Way Aerosol-Cloud
449 Interaction and Changes in Aerosol Size Distribution on Simulated Aerosol-Induced Deep
450 Convective Cloud Sensitivity, *J Atmos Sci*, 68, 685-698, doi: 10.1175/2010jas3651.1,
451 2011.
- 452 Fan, J. W., Zhang, R. Y., Li, G. H., and Tao, W. K.: Effects of aerosols and relative humidity on
453 cumulus clouds, *J Geophys Res-Atmos*, 112, D14204, doi: 10.1029/2006jd008136, 2007.
- 454 Fan, J. W., Yuan, T. L., Comstock, J. M., Ghan, S., Khain, A., Leung, L. R., Li, Z. Q., Martins, V.
455 J., and Ovchinnikov, M.: Dominant role by vertical wind shear in regulating aerosol effects



- 456 on deep convective clouds, *J Geophys Res-Atmos*, 114, D22206, doi:
457 10.1029/2009jd012352, 2009.
- 458 Fan, J. W., Leung, L. R., Li, Z. Q., Morrison, H., Chen, H. B., Zhou, Y. Q., Qian, Y., and Wang,
459 Y.: Aerosol impacts on clouds and precipitation in eastern China: Results from bin and
460 bulk microphysics, *J Geophys Res-Atmos*, 117, D00k36, doi: 10.1029/2011jd016537,
461 2012a.
- 462 Fan, J. W., Rosenfeld, D., Ding, Y. N., Leung, L. R., and Li, Z. Q.: Potential aerosol indirect effects
463 on atmospheric circulation and radiative forcing through deep convection, *Geophys Res*
464 *Lett*, 39, L09806, doi: 10.1029/2012gl051851, 2012b.
- 465 Fan, J. W., Leung, L. R., Rosenfeld, D., Chen, Q., Li, Z. Q., Zhang, J. Q., and Yan, H. R.:
466 Microphysical effects determine macrophysical response for aerosol impacts on deep
467 convective clouds, *P Natl Acad Sci USA*, 110, E4581-E4590, doi:
468 10.1073/pnas.1316830110, 2013.
- 469 Fan, J. W., Wang, Y., Rosenfeld, D., and Liu, X. H.: Review of Aerosol-Cloud Interactions:
470 Mechanisms, Significance, and Challenges, *J Atmos Sci*, 73, 4221-4252, doi: 10.1175/Jas-
471 D-16-0037.1, 2016.
- 472 Fan, J. W., Han, B., Varble, A., Morrison, H., North, K., Kollias, P., Chen, B. J., Dong, X. Q.,
473 Giangrande, S. E., Khain, A., Lin, Y., Mansell, E., Milbrandt, J. A., Stenz, R., Thompson,
474 G., and Wang, Y.: Cloud-resolving model intercomparison of an MC3E squall line case:
475 Part I-Convective updrafts, *J Geophys Res-Atmos*, 122, 9351-9378, doi:
476 10.1002/2017jd026622, 2017.
- 477 Fan, J. W., Rosenfeld, D., Zhang, Y. W., Giangrande, S. E., Li, Z. Q., Machado, L. A. T., Martin,
478 S. T., Yang, Y., Wang, J., Artaxo, P., Barbosa, H. M. J., Braga, R. C., Comstock, J. M.,



- 479 Feng, Z., Gao, W. H., Gomes, H. B., Mei, F., Pohlker, C., Pohlker, M. L., Poschl, U., and
480 de Souza, R. A. F.: Substantial convection and precipitation enhancements by ultrafine
481 aerosol particles, *Science*, 359, 411-418, doi: 10.1126/science.aan8461, 2018.
- 482 Fast, J. D., Gustafson, W. I., Easter, R. C., Zaveri, R. A., Barnard, J. C., Chapman, E. G., Grell, G.
483 A., and Peckham, S. E.: Evolution of ozone, particulates, and aerosol direct radiative
484 forcing in the vicinity of Houston using a fully coupled meteorology-chemistry-aerosol
485 model, *J Geophys Res-Atmos*, 111, D21305, doi: 10.1029/2005jd006721, 2006.
- 486 Gao, W. H., Fan, J. W., Easter, R. C., Yang, Q., Zhao, C., and Ghan, S. J.: Coupling spectral-bin
487 cloud microphysics with the MOSAIC aerosol model in WRF-Chem: Methodology and
488 results for marine stratocumulus clouds, *J Adv Model Earth Sy*, 8, 1289-1309, doi:
489 10.1002/2016ms000676, 2016.
- 490 Gelaro, R., McCarty, W., Suarez, M. J., Todling, R., Molod, A., Takacs, L., Randles, C. A.,
491 Darmenov, A., Bosilovich, M. G., Reichle, R., Wargan, K., Coy, L., Cullather, R., Draper,
492 C., Akella, S., Buchard, V., Conaty, A., da Silva, A. M., Gu, W., Kim, G. K., Koster, R.,
493 Lucchesi, R., Merkova, D., Nielsen, J. E., Partyka, G., Pawson, S., Putman, W., Rienecker,
494 M., Schubert, S. D., Sienkiewicz, M., and Zhao, B.: The Modern-Era Retrospective
495 Analysis for Research and Applications, Version 2 (MERRA-2), *J Climate*, 30, 5419-5454,
496 doi: 10.1175/Jcli-D-16-0758.1, 2017.
- 497 Grell, G. A., Peckham, S. E., Schmitz, R., McKeen, S. A., Frost, G., Skamarock, W. C., and Eder,
498 B.: Fully coupled "online" chemistry within the WRF model, *Atmos Environ*, 39, 6957-
499 6975, doi: 10.1016/j.atmosenv.2005.04.027, 2005.
- 500 Guenther, A., Karl, T., Harley, P., Wiedinmyer, C., Palmer, P. I., and Geron, C.: Estimates of
501 global terrestrial isoprene emissions using MEGAN (Model of Emissions of Gases and



- 502 Aerosols from Nature), Atmos Chem Phys, 6, 3181-3210, doi: 10.5194/acp-6-3181-2006,
503 2006.
- 504 Haywood, J., and Boucher, O.: Estimates of the direct and indirect radiative forcing due to
505 tropospheric aerosols: A review, Rev Geophys, 38, 513-543, doi: 10.1029/1999rg000078,
506 2000.
- 507 Houze, R. A.: Cloud dynamics, 2. edn., Elsevier/Acad. Press, Amsterdam, 2014.
- 508 Iacono, M. J., Delamere, J. S., Mlawer, E. J., Shephard, M. W., Clough, S. A., and Collins, W. D.:
509 Radiative forcing by long-lived greenhouse gases: Calculations with the AER radiative
510 transfer models, J Geophys Res-Atmos, 113, D13103, doi: 10.1029/2008jd009944, 2008.
- 511 Janjic, Z. I.: The Step-Mountain Eta Coordinate Model - Further Developments of the Convection,
512 Viscous Sublayer, and Turbulence Closure Schemes, Mon Weather Rev, 122, 927-945, doi:
513 10.1175/1520-0493(1994)122<0927:Tsmecm>2.0.Co;2, 1994.
- 514 Khain, A., Pokrovsky, A., Pinsky, M., Seifert, A., and Phillips, V.: Simulation of effects of
515 atmospheric aerosols on deep turbulent convective clouds using a spectral microphysics
516 mixed-phase cumulus cloud model. Part I: Model description and possible applications, J
517 Atmos Sci, 61, 2963-2982, doi: 10.1175/Jas-3350.1, 2004.
- 518 Khain, A., Rosenfeld, D., and Pokrovsky, A.: Aerosol impact on the dynamics and microphysics
519 of deep convective clouds, Q J Roy Meteor Soc, 131, 2639-2663, doi: 10.1256/qj.04.62,
520 2005.
- 521 Khain, A., and Lynn, B.: Simulation of a supercell storm in clean and dirty atmosphere using
522 weather research and forecast model with spectral bin microphysics, J Geophys Res-Atmos,
523 114, D19209, doi: 10.1029/2009jd011827, 2009.



- 524 Khain, A., Lynn, B., and Dudhia, J.: Aerosol Effects on Intensity of Landfalling Hurricanes as
525 Seen from Simulations with the WRF Model with Spectral Bin Microphysics, *J Atmos Sci*,
526 67, 365-384, doi: 10.1175/2009jas3210.1, 2010.
- 527 Khain, A. P., BenMoshe, N., and Pokrovsky, A.: Factors determining the impact of aerosols on
528 surface precipitation from clouds: An attempt at classification, *J Atmos Sci*, 65, 1721-1748,
529 doi: 10.1175/2007jas2515.1, 2008.
- 530 Khain, A. P., Leung, L. R., Lynn, B., and Ghan, S.: Effects of aerosols on the dynamics and
531 microphysics of squall lines simulated by spectral bin and bulk parameterization schemes,
532 *J Geophys Res-Atmos*, 114, D22203, doi: 10.1029/2009jd011902, 2009.
- 533 Khain, A. P., Beheng, K. D., Heymsfield, A., Korolev, A., Krichak, S. O., Levin, Z., Pinsky, M.,
534 Phillips, V., Prabhakaran, T., Teller, A., van den Heever, S. C., and Yano, J. I.:
535 Representation of microphysical processes in cloud-resolving models: Spectral (bin)
536 microphysics versus bulk parameterization, *Rev Geophys*, 53, 247-322, doi:
537 10.1002/2014rg000468, 2015.
- 538 Koren, I., Dagan, G., and Altaratz, O.: From aerosol-limited to invigoration of warm convective
539 clouds, *Science*, 344, 1143-1146, doi: 10.1126/science.1252595, 2014.
- 540 Lebo, Z.: A Numerical Investigation of the Potential Effects of Aerosol-Induced Warming and
541 Updraft Width and Slope on Updraft Intensity in Deep Convective Clouds, *J Atmos Sci*,
542 75, 535-554, doi: 10.1175/Jas-D-16-0368.1, 2018.
- 543 Lebo, Z. J., and Seinfeld, J. H.: Theoretical basis for convective invigoration due to increased
544 aerosol concentration, *Atmos Chem Phys*, 11, 5407-5429, doi: 10.5194/acp-11-5407-2011,
545 2011.



- 546 Lebo, Z. J., Morrison, H., and Seinfeld, J. H.: Are simulated aerosol-induced effects on deep
547 convective clouds strongly dependent on saturation adjustment? *Atmos Chem Phys*, 12,
548 9941-9964, doi: 10.5194/acp-12-9941-2012, 2012.
- 549 Lee, S. S., Li, Z. Q., Zhang, Y. W., Yoo, H., Kim, S., Kim, B. G., Choi, Y. S., Mok, J., Um, J.,
550 Choi, K. O., and Dong, D. H.: Effects of model resolution and parameterizations on the
551 simulations of clouds, precipitation, and their interactions with aerosols, *Atmos Chem Phys*,
552 18, 13-29, doi: 10.5194/acp-18-13-2018, 2018.
- 553 Li, G. H., Wang, Y., and Zhang, R. Y.: Implementation of a two-moment bulk microphysics
554 scheme to the WRF model to investigate aerosol-cloud interaction, *J Geophys Res-Atmos*,
555 113, D15211, doi: 10.1029/2007jd009361, 2008.
- 556 Li, X. W., Tao, W. K., Khain, A. P., Simpson, J., and Johnson, D. E.: Sensitivity of a Cloud-
557 Resolving Model to Bulk and Explicit Bin Microphysical Schemes. Part I: Comparisons, *J*
558 *Atmos Sci*, 66, 3-21, doi: 10.1175/2008jas2646.1, 2009.
- 559 Li, Z. Q., Niu, F., Fan, J. W., Liu, Y. G., Rosenfeld, D., and Ding, Y. N.: Long-term impacts of
560 aerosols on the vertical development of clouds and precipitation, *Nat Geosci*, 4, 888-894,
561 doi: 10.1038/Ngeo1313, 2011.
- 562 Loftus, A. M., and Cotton, W. R.: Examination of CCN impacts on hail in a simulated supercell
563 storm with triple-moment hail bulk microphysics, *Atmos Res*, 147, 183-204, doi:
564 10.1016/j.atmosres.2014.04.017, 2014.
- 565 Lohmann, U., and Feichter, J.: Global indirect aerosol effects: a review, *Atmos Chem Phys*, 5,
566 715-737, doi: 10.5194/acp-5-715-2005, 2005.



- 567 Milbrandt, J. A., and Yau, M. K.: A multimoment bulk microphysics parameterization. Part II: A
568 proposed three-moment closure and scheme description, *J Atmos Sci*, 62, 3065-3081, doi:
569 10.1175/Jas3535.1, 2005.
- 570 Morrison, H., Curry, J. A., and Khvorostyanov, V. I.: A new double-moment microphysics
571 parameterization for application in cloud and climate models. Part I: Description, *J Atmos*
572 *Sci*, 62, 1665-1677, doi: 10.1175/Jas3446.1, 2005.
- 573 Morrison, H., Thompson, G., and Tatarskii, V.: Impact of Cloud Microphysics on the Development
574 of Trailing Stratiform Precipitation in a Simulated Squall Line: Comparison of One- and
575 Two-Moment Schemes, *Mon Weather Rev*, 137, 991-1007, doi: 10.1175/2008mwr2556.1,
576 2009.
- 577 Morrison, H., and Milbrandt, J.: Comparison of Two-Moment Bulk Microphysics Schemes in
578 Idealized Supercell Thunderstorm Simulations, *Mon Weather Rev*, 139, 1103-1130, doi:
579 10.1175/2010mwr3433.1, 2011.
- 580 Morrison, H.: On the robustness of aerosol effects on an idealized supercell storm simulated with
581 a cloud system-resolving model, *Atmos Chem Phys*, 12, 7689-7705, doi: 10.5194/acp-12-
582 7689-2012, 2012.
- 583 Rosenfeld, D., Lohmann, U., Raga, G. B., O'Dowd, C. D., Kulmala, M., Fuzzi, S., Reissell, A.,
584 and Andreae, M. O.: Flood or drought: How do aerosols affect precipitation?, *Science*, 321,
585 1309-1313, doi: 10.1126/science.1160606, 2008.
- 586 Rosenfeld, D., Andreae, M. O., Asmi, A., Chin, M., de Leeuw, G., Donovan, D. P., Kahn, R.,
587 Kinne, S., Kivekas, N., Kulmala, M., Lau, W., Schmidt, K. S., Suni, T., Wagner, T., Wild,
588 M., and Quaas, J.: Global observations of aerosol-cloud-precipitation-climate interactions,
589 *Rev Geophys*, 52, 750-808, doi: 10.1002/2013rg000441, 2014.



- 590 Rosenfeld, D., Zheng, Y. T., Hashimshoni, E., Pohlker, M. L., Jefferson, A., Pohlker, C., Yu, X.,
591 Zhu, Y. N., Liu, G. H., Yue, Z. G., Fischman, B., Li, Z. Q., Giguzin, D., Goren, T., Artaxo,
592 P., Barbosa, H. M. J., Poschl, U., and Andreae, M. O.: Satellite retrieval of cloud
593 condensation nuclei concentrations by using clouds as CCN chambers, *P Natl Acad Sci*
594 *USA*, 113, 5828-5834, doi: 10.1073/pnas.1514044113, 2016.
- 595 Salamanca, F., and Martilli, A.: A new Building Energy Model coupled with an Urban Canopy
596 Parameterization for urban climate simulations-part II. Validation with one dimension off-
597 line simulations, *Theor Appl Climatol*, 99, 345-356, doi: 10.1007/s00704-009-0143-8,
598 2010.
- 599 Sheffield, A. M., Saleeby, S. M., and van den Heever, S. C.: Aerosol-induced mechanisms for
600 cumulus congestus growth, *J Geophys Res-Atmos*, 120, 8941-8952, doi:
601 10.1002/2015jd023743, 2015.
- 602 Skamarock, W. C., Klemp, J. B., Dudhia, J., Gill, D. O., Barker, D. M., Duda, M., Huang, X. Y.,
603 Wang, W., and Powers, J. G.: A description of the advanced research WRF version 3,
604 NCAR, Tech. Note, Mesoscale and Microscale Meteorology Division, National Center
605 for Atmospheric Research, Boulder, Colorado, USA, 2008.
- 606 Storer, R. L., van den Heever, S. C., and Stephens, G. L.: Modeling Aerosol Impacts on Convective
607 Storms in Different Environments, *J Atmos Sci*, 67, 3904-3915, doi:
608 10.1175/2010jas3363.1, 2010.
- 609 Wang, Y., Fan, J. W., Zhang, R. Y., Leung, L. R., and Franklin, C.: Improving bulk microphysics
610 parameterizations in simulations of aerosol effects, *J Geophys Res-Atmos*, 118, 5361-5379,
611 doi: 10.1002/jgrd.50432, 2013.



- 612 Wiedinmyer, C., Akagi, S. K., Yokelson, R. J., Emmons, L. K., Al-Saadi, J. A., Orlando, J. J., and
613 Soja, A. J.: The Fire INventory from NCAR (FINN): a high resolution global model to
614 estimate the emissions from open burning, *Geosci Model Dev*, 4, 625-641, doi:
615 10.5194/gmd-4-625-2011, 2011.
- 616 Yuan, T. L., Li, Z. Q., Zhang, R. Y., and Fan, J. W.: Increase of cloud droplet size with aerosol
617 optical depth: An observation and modeling study, *J Geophys Res-Atmos*, 113, D04201,
618 doi: 10.1029/2007jd008632, 2008.
- 619 Zaveri, R. A., Easter, R. C., Fast, J. D., and Peters, L. K.: Model for Simulating Aerosol
620 Interactions and Chemistry (MOSAIC), *J Geophys Res-Atmos*, 113, D13204, doi:
621 10.1029/2007jd008782, 2008.
- 622



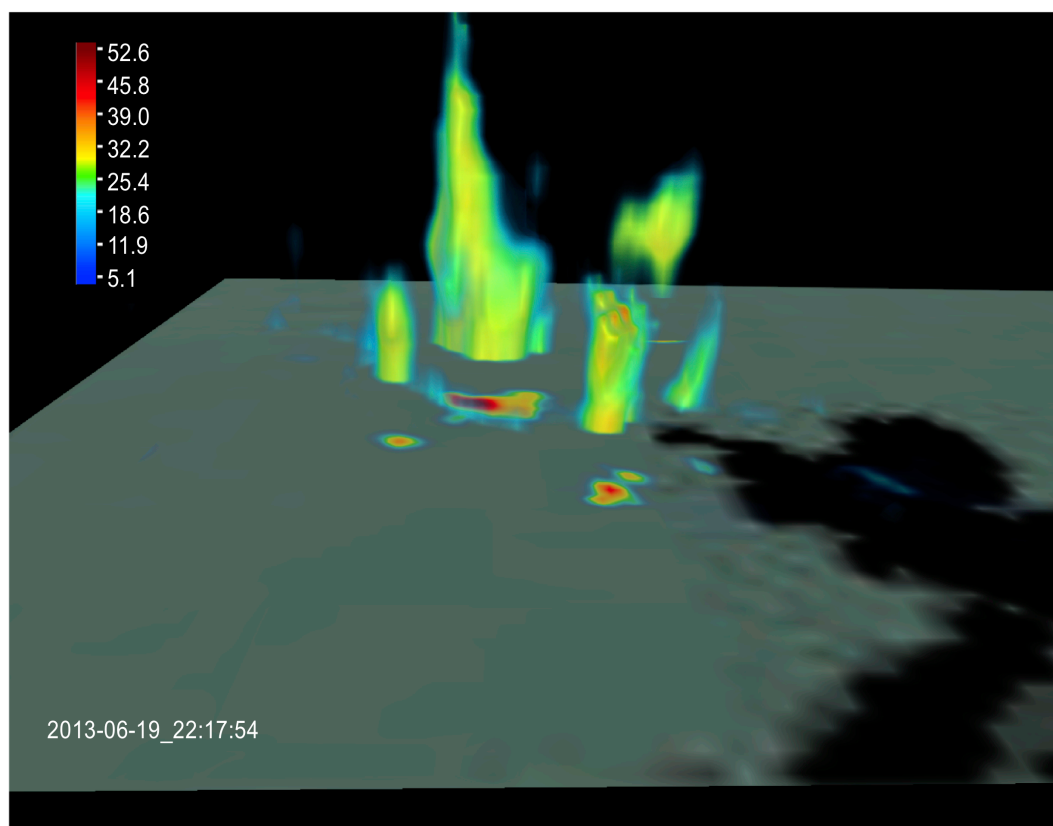
623 **Table 1** Descriptions of the PM_{2.5} Monitoring Sites over the Houston area from TCEQ

Abbreviation	Site Descriptions	Latitude	Longitude
HA	Houston Aldine	29.901	-95.326
HDP	Houston Deer Park 2	29.670	-95.129
SFP	Seabrook Friendship Park	29.583	-95.016
CR	Conroe Relocated	30.350	-95.425
KW	Kingwood	30.058	-95.190
CT	Clinton	29.734	-95.258
PP	Park Place	29.686	-95.294
GS	Galveston 99th Street	29.254	-94.861

624

625

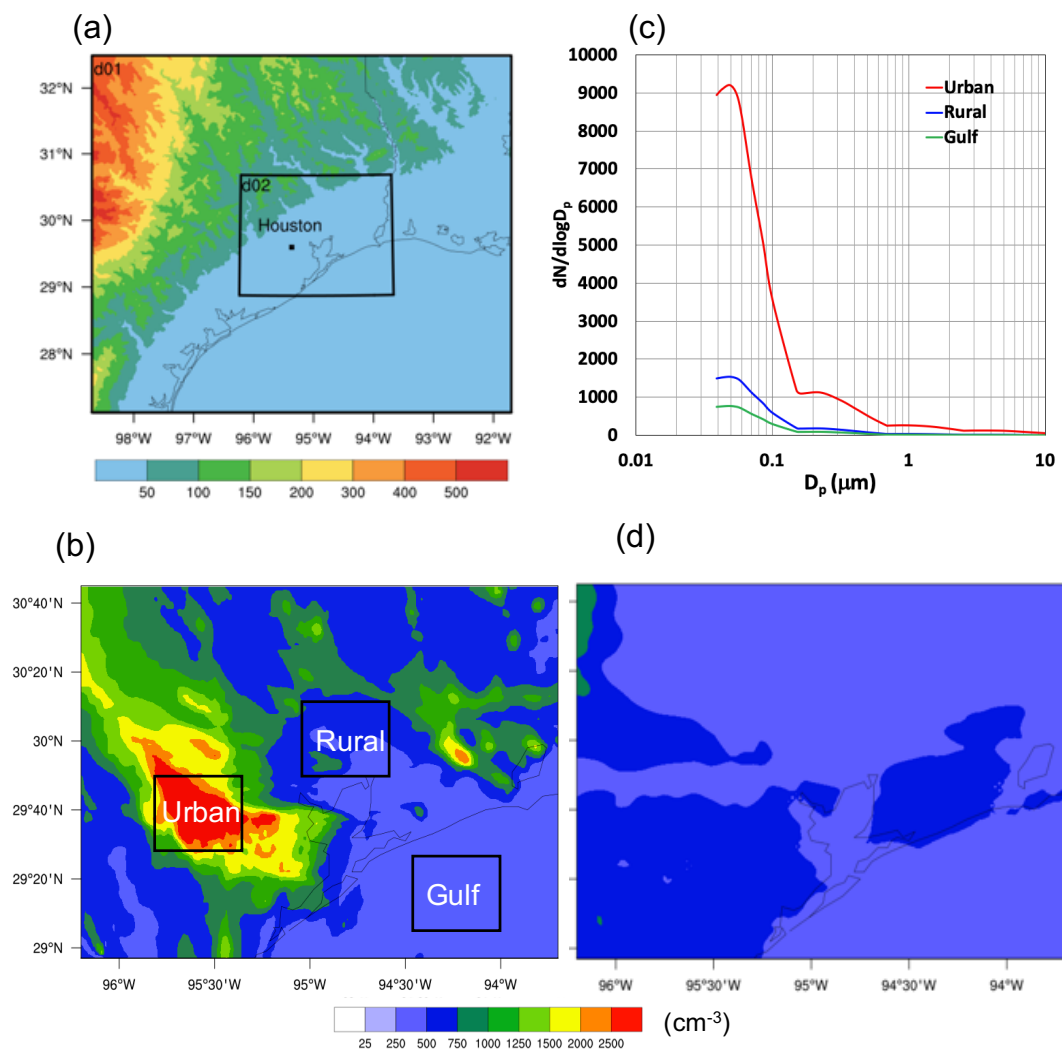
626



627

628 **Figure 1** 3D structure snapshot of radar reflectivity (unit: dBZ) from NEXRAD, overlaid with the
629 composite reflectivity shown on the surface at the time when the maximum reflectivity is observed
630 (2217 UTC). The dark shade shows the water body and the largest cell is in the Houston.

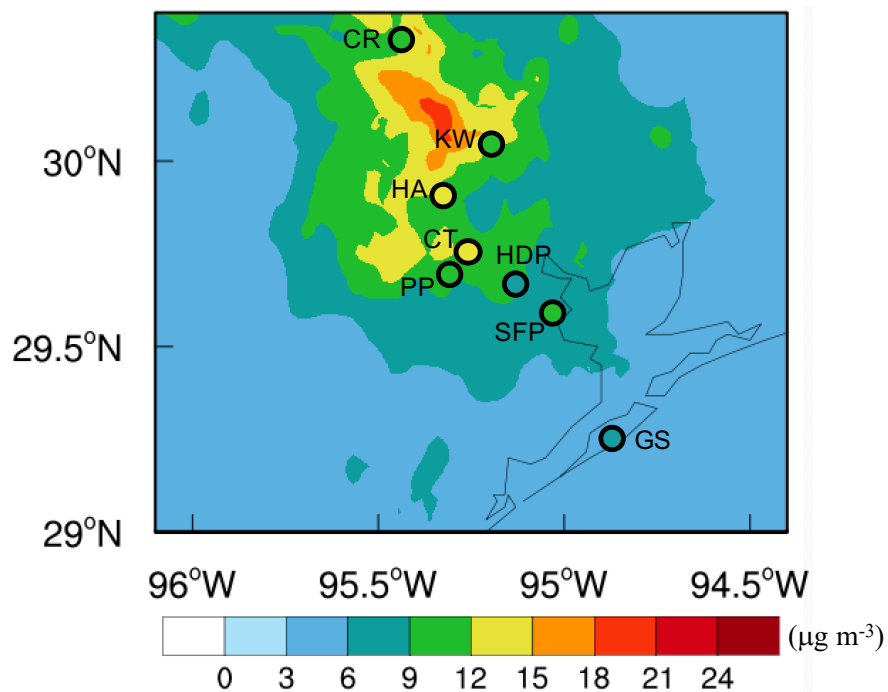
631



632

633 **Figure 2** (a) Simulation domains with the terrain heights (unit: m), (b) aerosol number
634 concentration (unit: cm⁻³) from D1_MOR_anth, (c) aerosol size distributions over the urban, rural,
635 and Gulf of Mexico as marked by three black boxes in Fig. 2b at 1200 UTC, 19 Jun 2013 (6-hr
636 before the convection initiation), and (d) the same as Fig. 2b, but for D1_MOR_noanth in which
637 the anthropogenic aerosols are excluded.

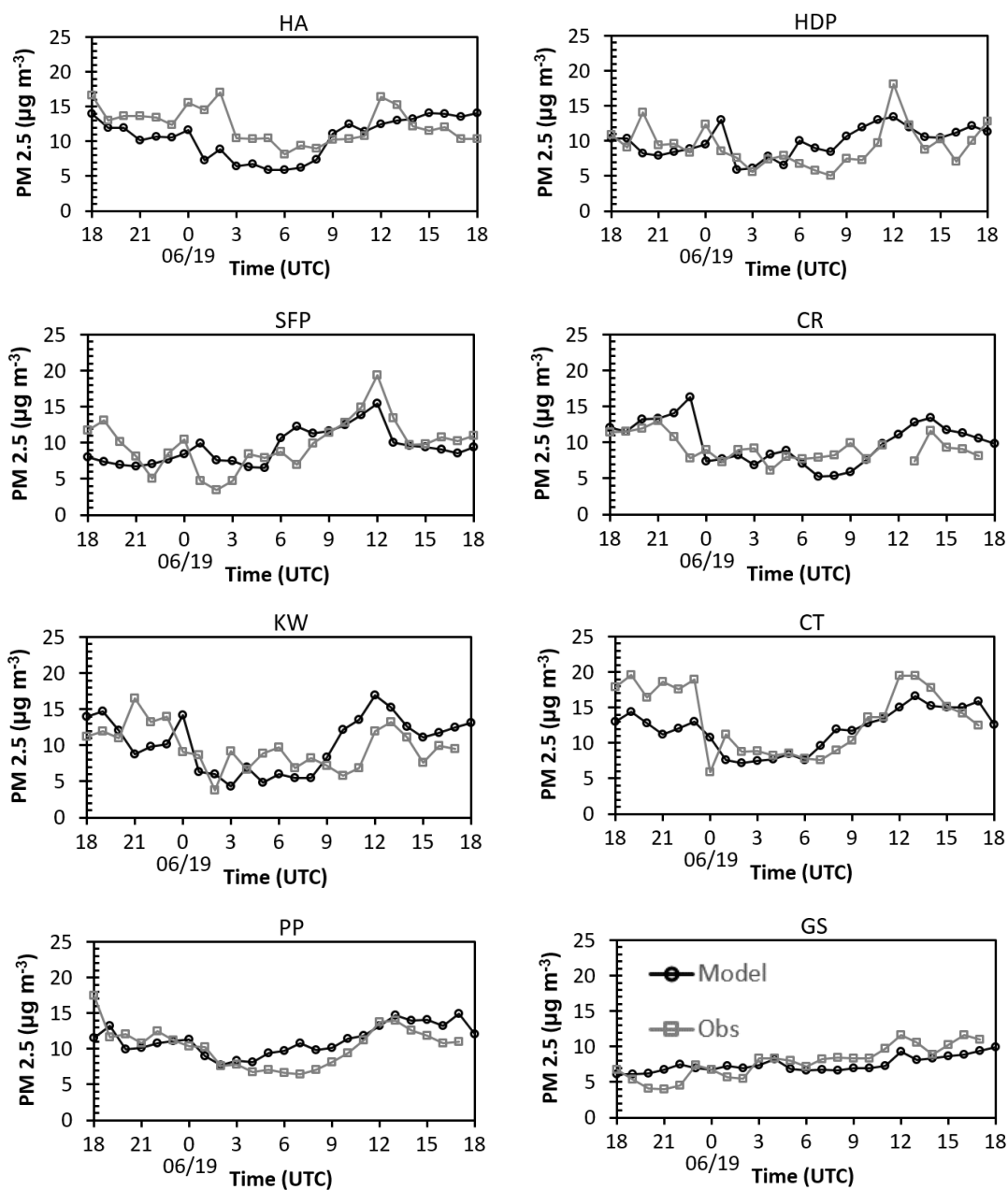
638



639

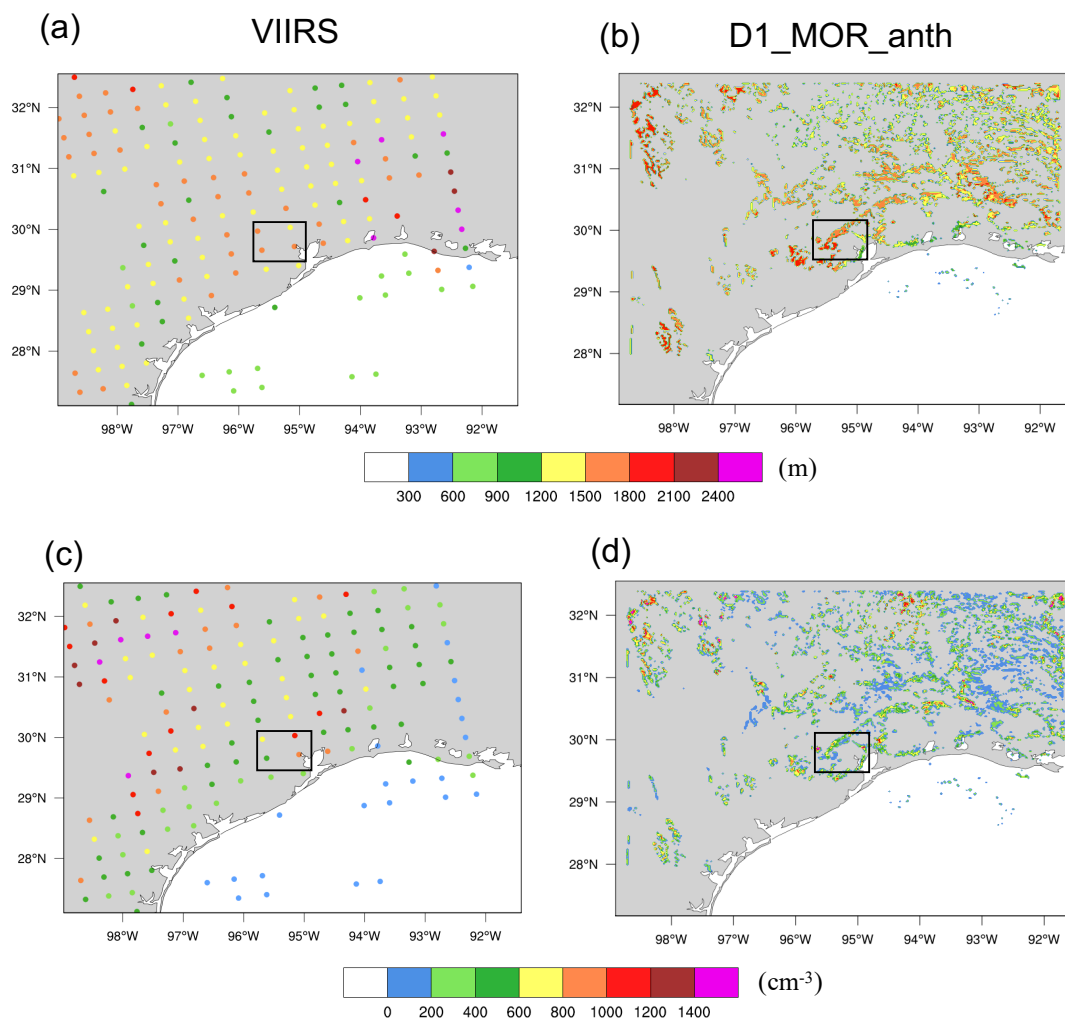
640 **Figure 3** Comparisons of 24-hr averaged PM_{2.5} mass concentrations (unit: $\mu\text{g m}^{-3}$) between model
641 simulation D1_MOR_anth (contoured) and site observation from TCEQ (colored circles) from
642 1800 UTC, 18 June 2013 to 1800 UTC, 19 June 2013 (1 day before the convection initiation). The
643 site names and other information are shown in Table 1.

644



645

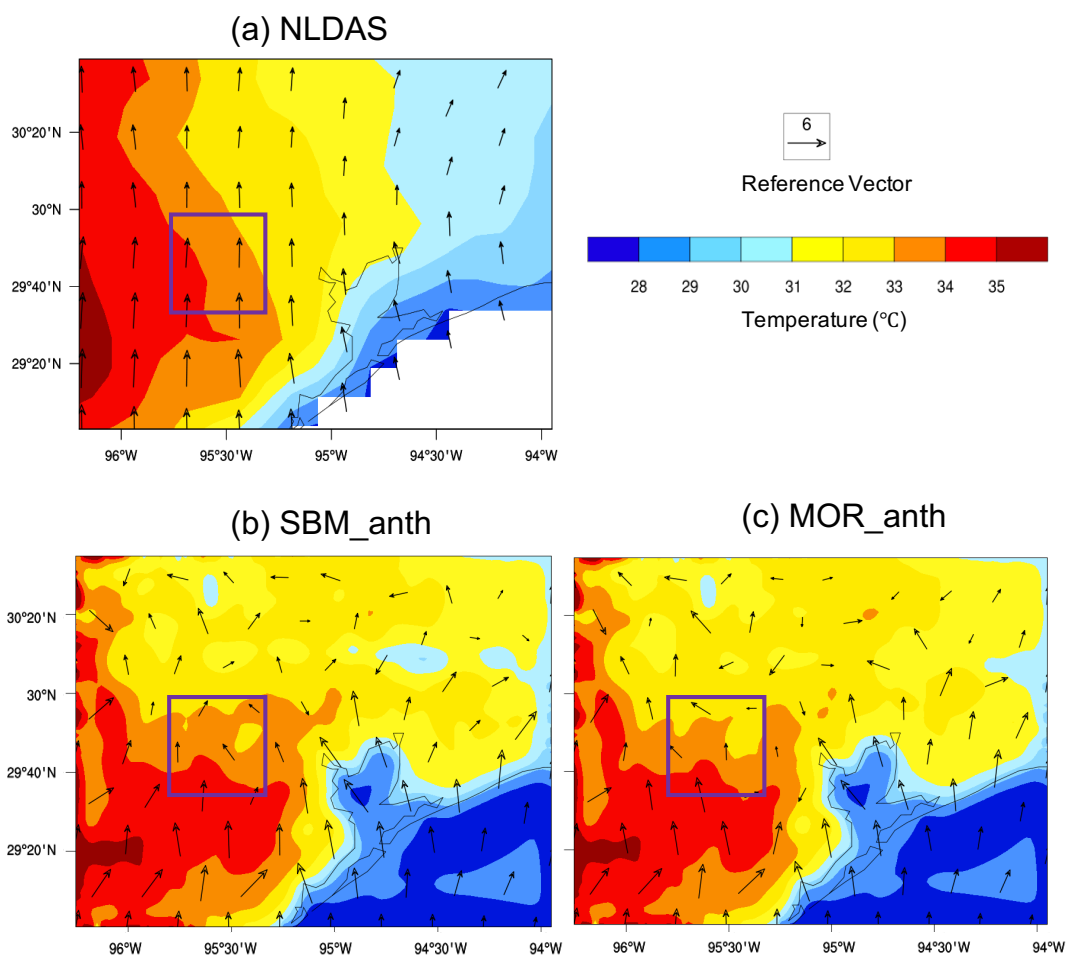
646 **Figure 4** Site-by-site comparisons of hourly PM_{2.5} mass concentrations (unit: $\mu\text{g m}^{-3}$) from
647 D1_MOR_anth and TCEQ site observation over 24 hours from 1800 UTC, 18 June 2013 to 1800
648 UTC, 19 June 2013 (1 day before the convection initiation).



649

650 **Figure 5** Evaluation of (a,b) cloud base heights (unit: m) and (c,d) CCN number concentration at
651 cloud base (unit: cm⁻³) from VIIRS satellite (left) retrieved at 1943 UTC (Rosenfeld et al. 2016)
652 and model simulation D1_MOR_anth (right) at 2000 UTC, 19 June 2013. The Houston area is
653 marked as the black box. Satellite-retrieved cloud base height was calculated from the difference
654 between reanalysis surface air temperature (from reanalysis data) and VIIRS-measured cloud base
655 temperature (warmest cloudy pixel) divided by the dry adiabatic lapse rate, while modeled cloud
656 base height was determined by the lowest cloud layer with cloud mass mixing ratio greater than
657 10⁻⁵ kg kg⁻¹.

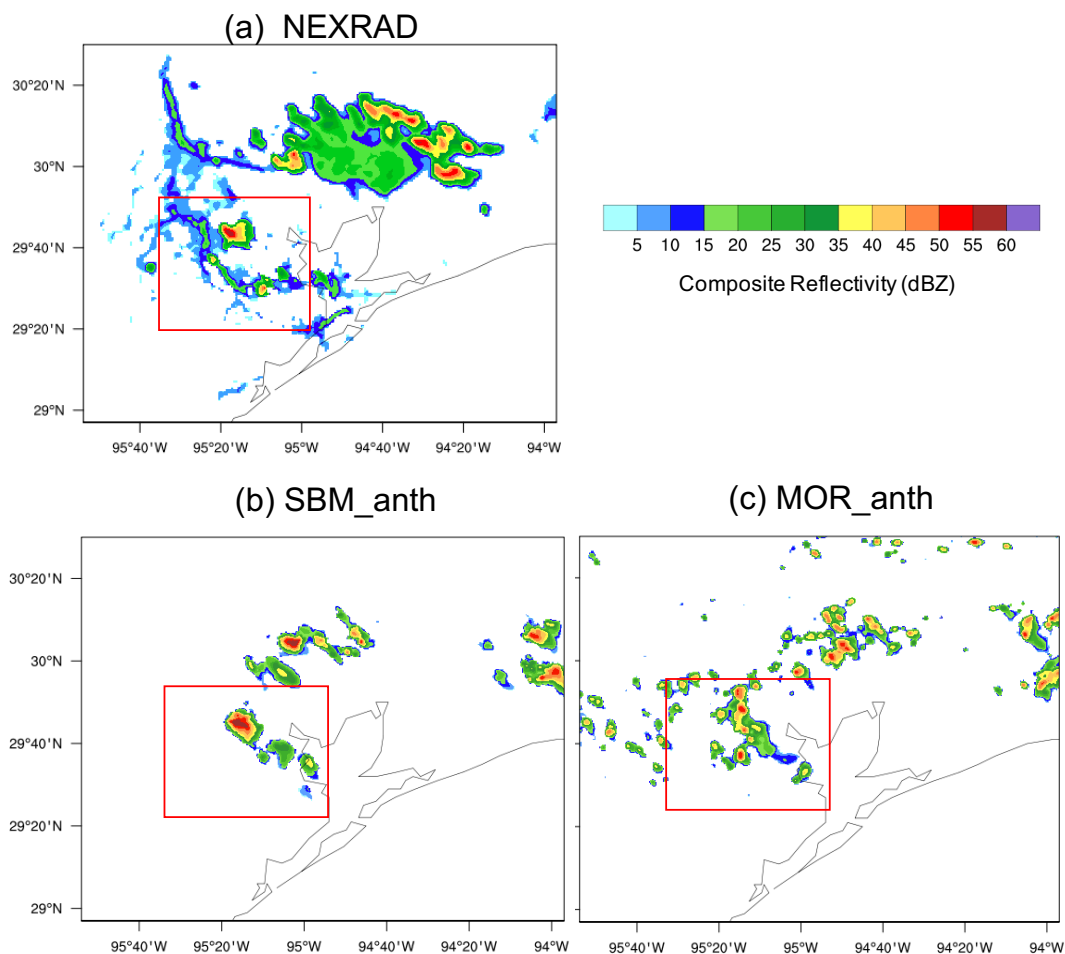
658



659

660 **Figure 6** 2-m Temperature (shaded; unit: °C) and 10-m winds (vectors; unit: m s^{-1}) from (a)
661 NLDAS, (b) SBM_anth and (c) MOR_anth at 1800 UTC, 19 Jun 2013. The purple box denotes
662 the Houston area.

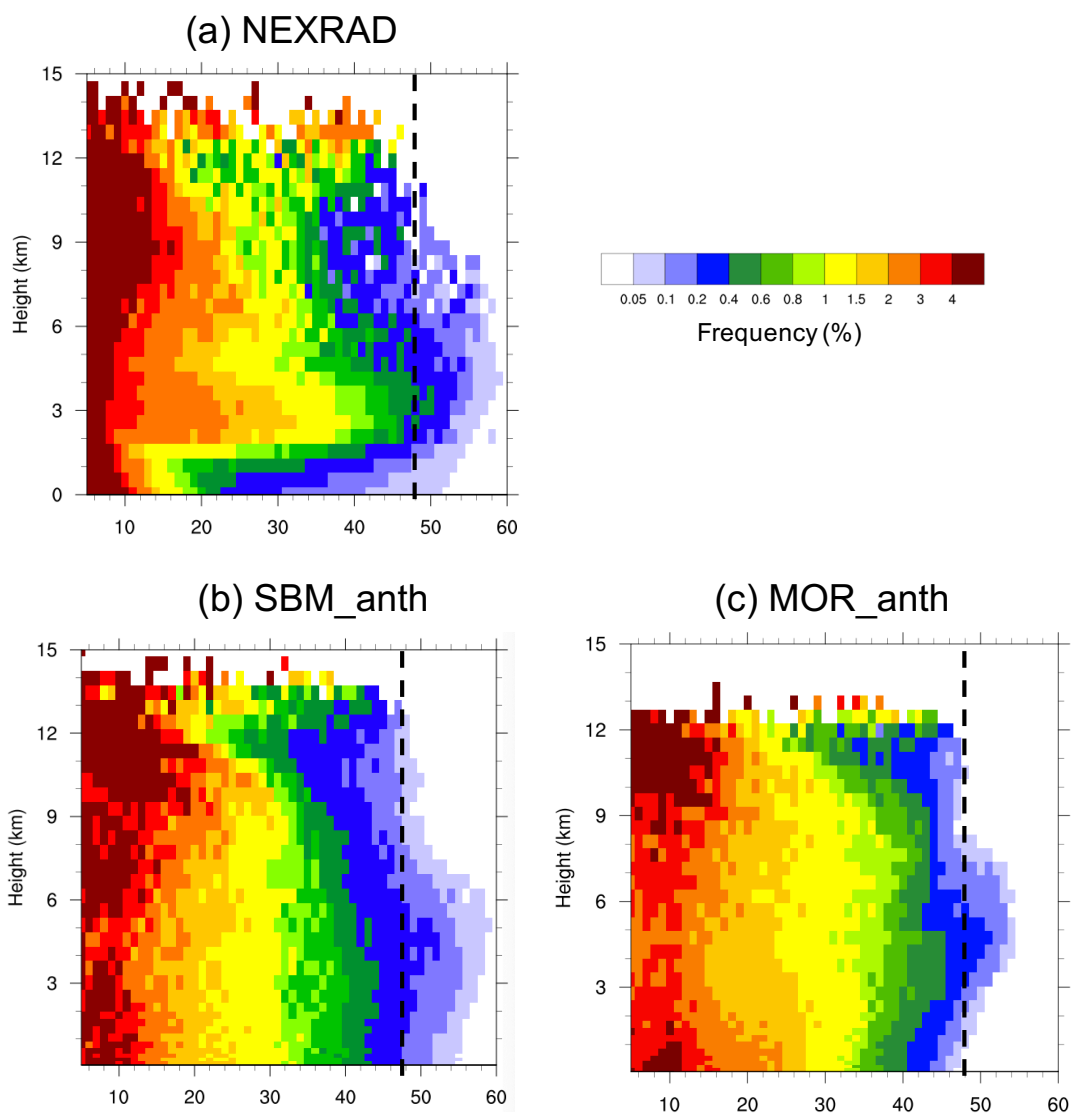
663



664

665 **Figure 7** Composite reflectivity (unit: dBZ) from (a) NEXRAD (2217 UTC), (b) SBM_anth
666 (2140 UTC) and (c) MOR_anth (2125 UTC) when maximum reflectivity in Houston is observed
667 on 19 June 2013. The red box is the study area for convection cells near Houston.

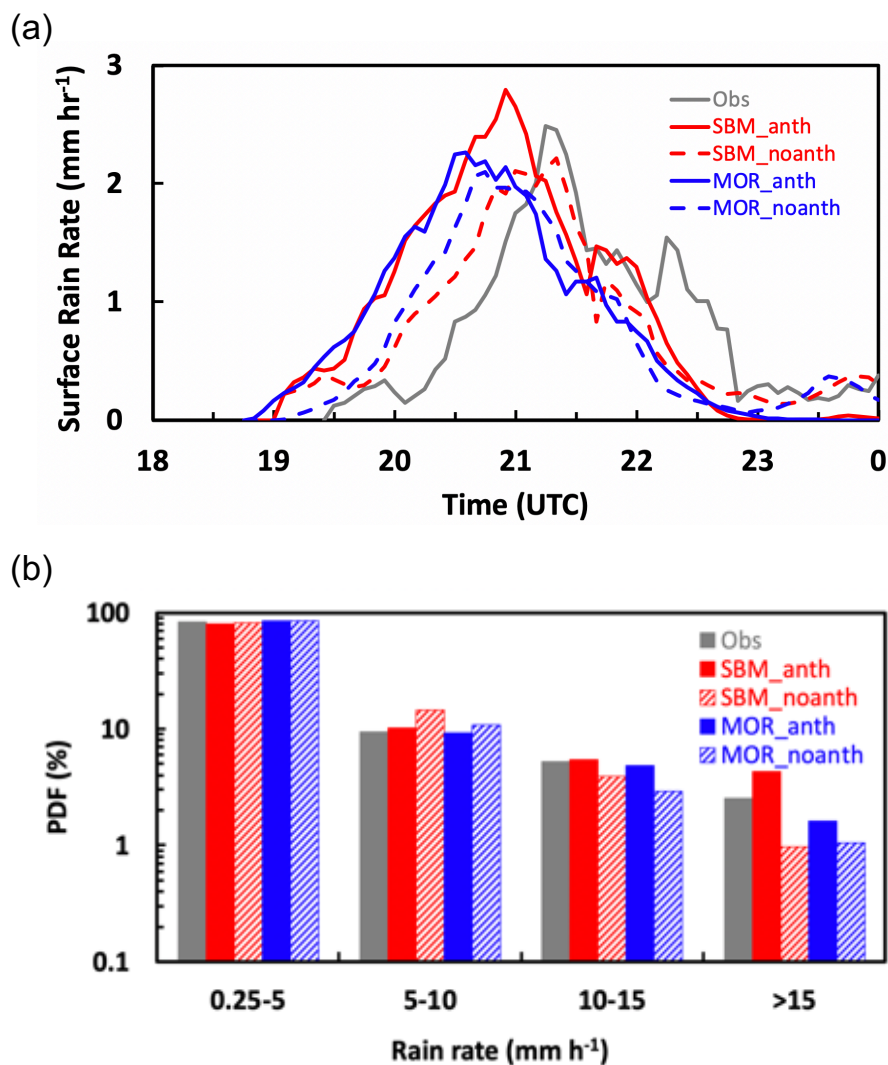
668



669

670 **Figure 8** The CFAD of reflectivity (unit: dBZ) for the values larger than 0 dBZ from (a) NEXRAD,
671 (b) SBM_anth and (c) MOR_anth over the study area (red box in Fig. 7) from 1800 UTC, 19 Jun
672 to 0000 UTC, 20 Jun 2013. The black solid lines denote the reflectivity with the value of 48 dBZ.

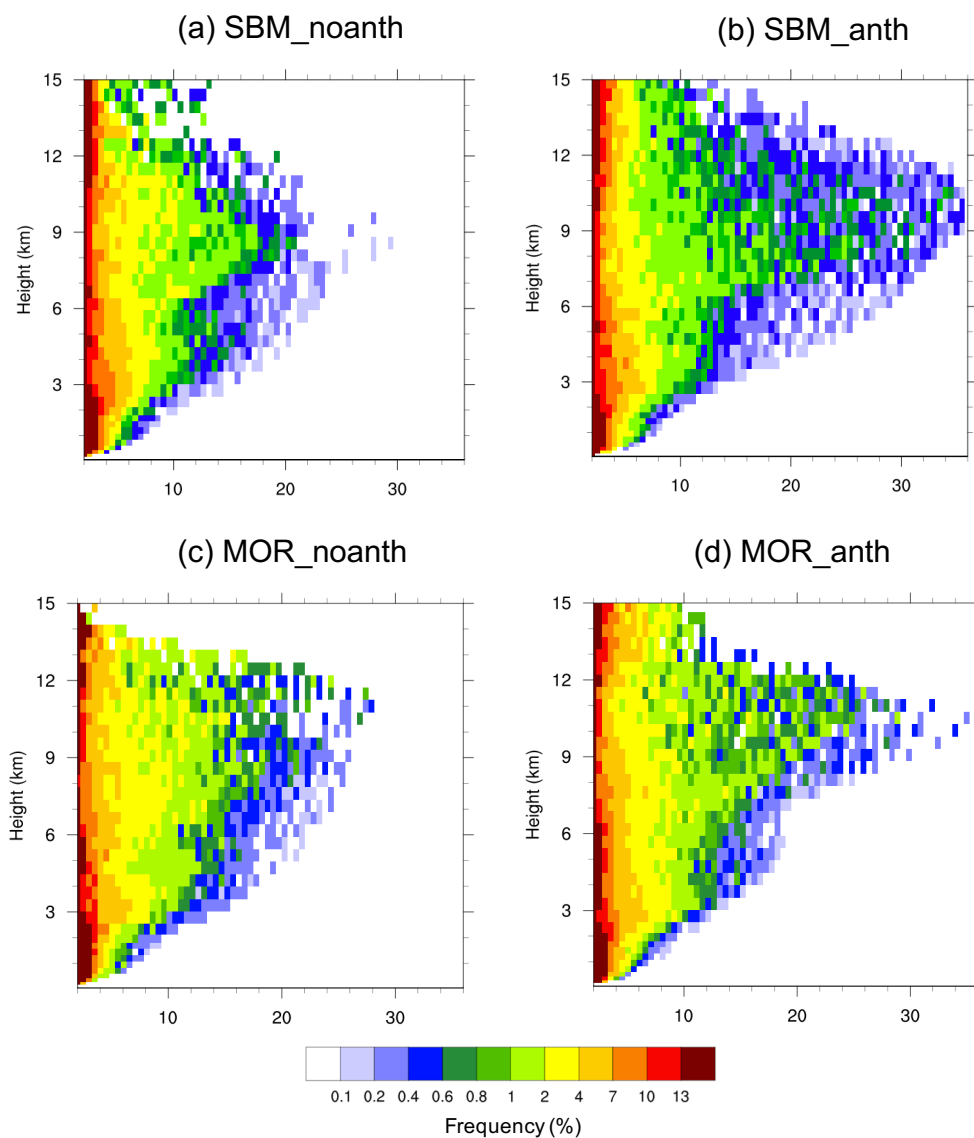
673



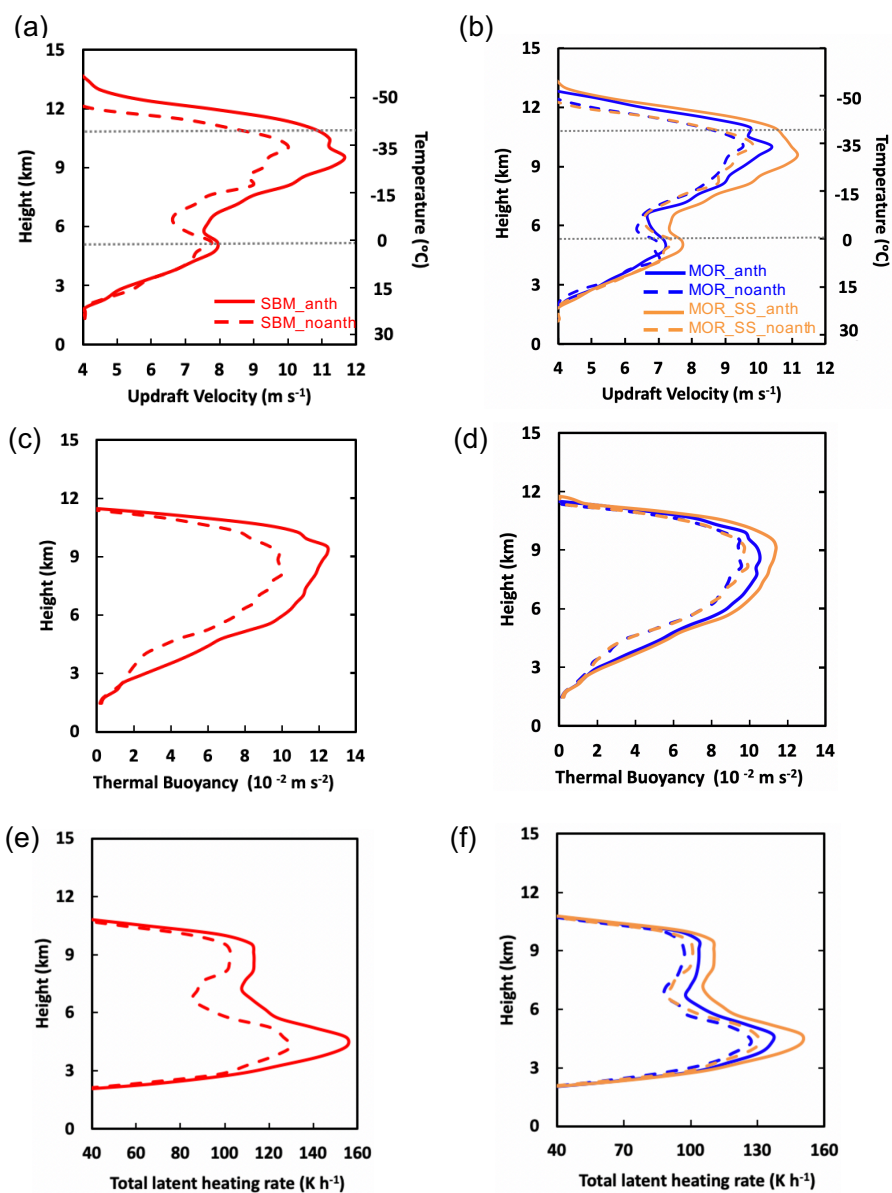
674

675 **Figure 9** (a) Time series of averaged surface rain rate (unit: mm h⁻¹) and (b) PDFs of rain rate for
676 the values larger than 0.25 mm h⁻¹ over the study area (red box in Fig. 7) from observation (grey),
677 SBM_anth and SBM_noanth (red), MOR_anth and MOR_noanth (blue) from 1800UTC, 19 Jun
678 2013 to 0000 UTC, 20 Jun 2013. The observed precipitation rate is obtained by NEXRAD
679 retrieved rain rate. Both observation and model data are in every 5-min frequency.

680



681
682 **Figure 10** CFADs of updraft velocity (unit: m s^{-1}) for values larger than 2 m s^{-1} from (a)
683 SBM_noanth, (b) SBM_anth, (c) MOR_noanth, and (d) MOR_anth over the study area (red box
684 in Fig. 7) during the strong convection period (2000 – 2300 UTC, 19 Jun 2013).

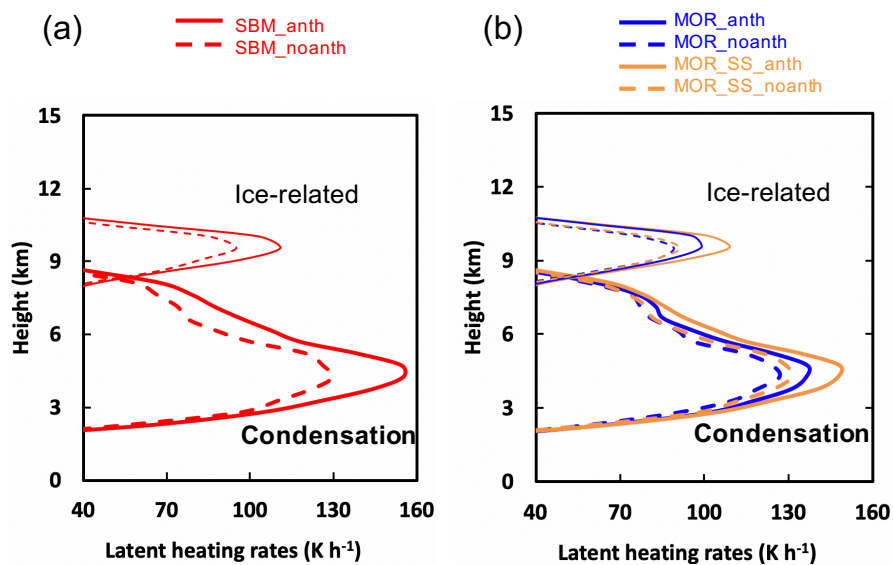


685

686 **Figure 11** Vertical profiles of (a,b) updraft velocity (unit: $m s^{-1}$), (c,d) thermal buoyancy (unit:
687 $m s^{-2}$) and (e,f) total latent heating rate (unit: $K h^{-1}$) averaged over the top 25 percentiles (i.e.,
688 from 75th to 100th) of the updrafts with velocity greater than $2 m s^{-1}$ from the simulations
689 SBM_anth and SBM_noanth (red), MOR_anth and MOR_noanth (blue), and MOR_SS_anth
690 and MOR_SS_noanth (orange) over the study area (red box in Fig. 7) during the strong



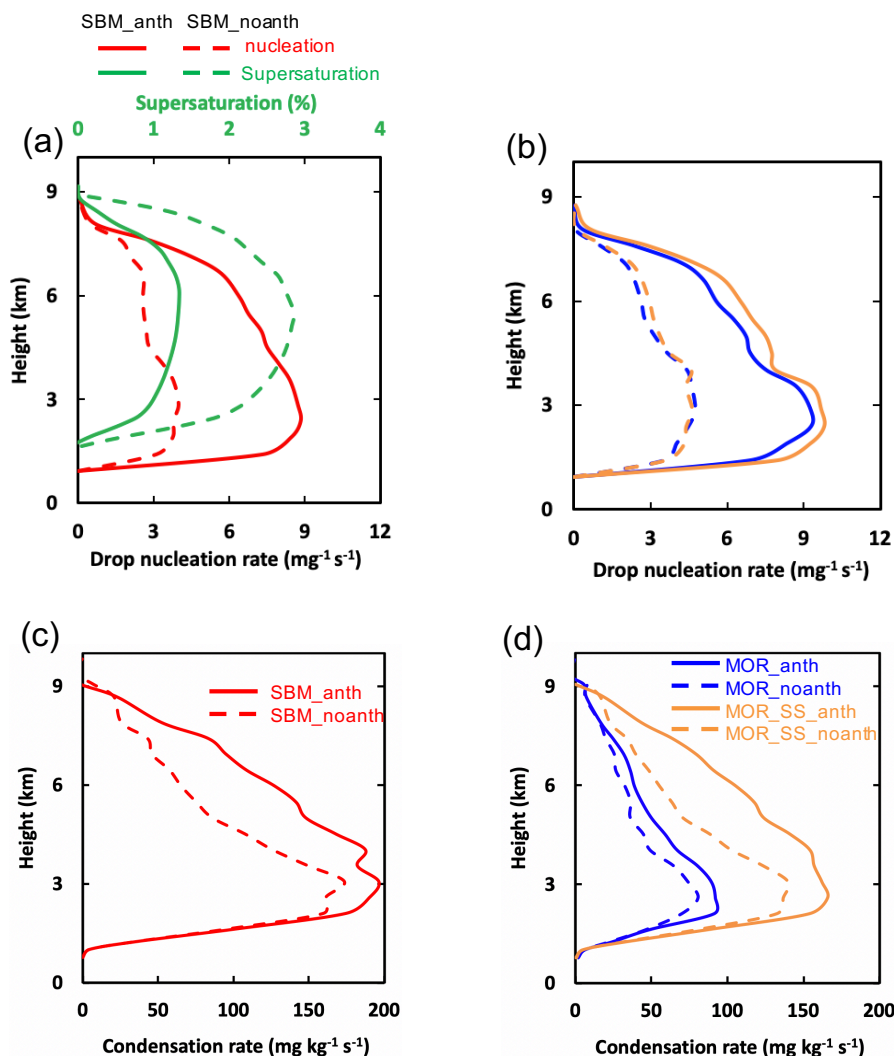
691 convection period (2000 – 2300 UTC, 19 Jun 2013). The dotted lines in (a) and (b) denote the
692 freezing level (0 °C) and homogeneous freezing level (-40 °C).
693



694

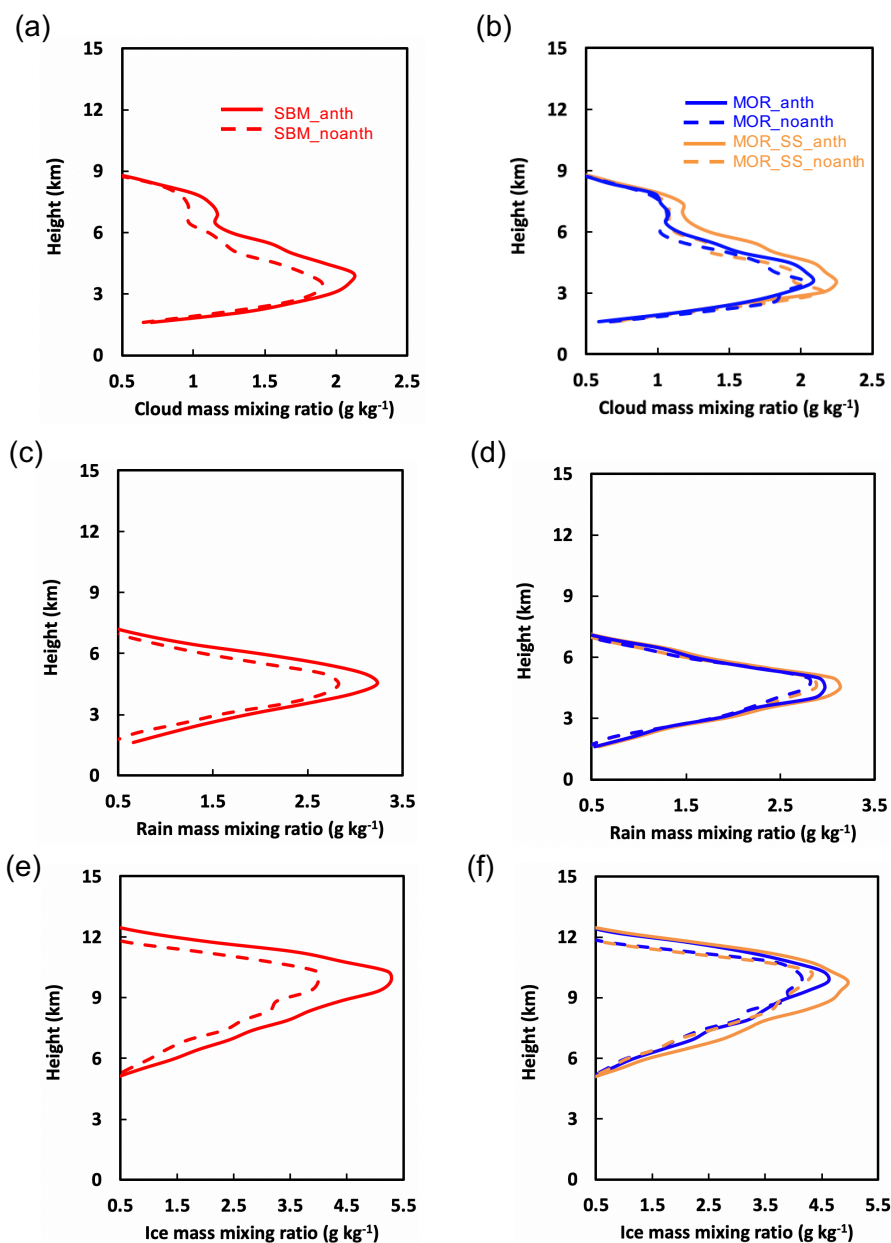
695 **Figure 12** Vertical profiles of condensation heating rate (thick lines below 9 km; unit: K h⁻¹) and
696 ice-related latent heating rate (thin lines above 9 km; unit: K h⁻¹) averaged over the top 25
697 percentiles (i.e., 75th to 100th) of the updrafts with velocity greater than 2 m s⁻¹ from the
698 simulations (a) SBM_anth and SBM_noanth (red), and (b) MOR_anth and MOR_noanth (blue),
699 and MOR_SS_anth and MOR_SS_noanth (orange) over the study area (red box in Fig. 7) during
700 the strong convection period (2000 – 2300 UTC, 19 Jun 2013).

701



702

703 **Figure 13** Vertical profiles of (a) drop nucleation rate (red; unit: $\text{mg}^{-1} \text{s}^{-1}$) and supersaturation
704 with respect to water (green; unit: %) from SBM_anth and SBM_noanth, (b) drop nucleation rate
705 (unit: $\text{mg}^{-1} \text{s}^{-1}$) from MOR_anth and MOR_noanth (blue), and MOR_SS_anth and
706 MOR_SS_noanth (orange), (c) condensation rate (unit: $\text{mg kg}^{-1} \text{s}^{-1}$) from SBM_anth and
707 SBM_noanth (red), and (d) the same as (c) but from MOR_anth and MOR_noanth (blue), and
708 MOR_SS_anth and MOR_SS_noanth (orange), averaged over the top 25 percentiles (i.e., from
709 75th to 100th) of the updrafts with velocity greater than 2 m s^{-1} over the study area (red box in
710 Fig. 7) during the strong convection period (2000 – 2300 UTC, 19 Jun 2013).



711

712 **Figure 14** Vertical profiles of (a, b) cloud droplet, (c, d) rain drop and (e, f) ice particle (including
713 ice, snow, and graupel) mass mixing ratios (unit: g kg^{-1}) averaged over the top 25 percentiles (i.e.,
714 75th to 100th) of the updrafts with value greater than 2 m s^{-1} from the simulations SBM_anth and
715 SBM_noanth (red), MOR_anth and MOR_noanth (blue), and MOR_SS_anth and



716 MOR_SS_noanth (orange) over the study area (red box in Fig. 7) during the strong convection
717 period (2000 – 2300 UTC, 19 Jun 2013).
718